Performance of the BL03U beamline at SSRF

Z. P. Sun,[a,b] **Z. H. Liu,**[a,b] **Z. T. Liu,**[a,b] **W. L. Liu,**[a,b,c] **F. Y. Zhang,**[a,b] **D. W. Shen,**[a,b,c] **M. Ye**[a,b]* **and S. Qiao**[a,b,c]*

[a]Center for Excellence in Superconducting Electronics, State Key Laboratory of Functional Materials for Informatics, Shanghai Institute of Microsystem and Information Technology, Chinese Academy of Sciences, Shanghai 200050, People's Republic of China, [b]Center of Materials Science and Optoelectronics Engineering, University of Chinese Academy of Sciences, Beijing 100049, People's Republic of China, and [c]School of Physical Science and Technology, ShanghaiTech University, Shanghai 201210, People's Republic of China.
*Correspondence e-mail: yemao@mail.sim.ac.cn, qiaoshan@mail.sim.ac.cn

The vacuum ultraviolet beamline BL03U with a photon energy range from 7 eV upwards has been constructed at the 3.5 GeV Shanghai Synchrotron Radiation Facility. Equipped with an APPLE-Knot undulator, this beamline is dedicated to angle-resolved photoemission spectroscopy. An energy-resolving power of higher than 4.6×10^4 has been achieved in the photon energy range 21.6–48 eV, which is almost the same as the theoretical estimation.

1. Introduction

Material science has developed tremendously in recent years due to rapidly improved experimental techniques based on synchrotron radiation light sources. In order to develop novel materials, it is necessary to have a fundamental understanding of how the functions of materials are related to their electronic structures as an origin of the physical properties of solids. The specific regime of very high energy resolution angle-resolved photoelectron spectroscopy (ARPES) has proven to be particularly successful for the measurement of electronic states at low binding energies in correlated electron systems (Damascelli *et al.*, 2003). However, owing to its surface sensitivity, ARPES could only be used to observe the electronic structure near the surface, due to the relatively short mean free path of photoelectrons (Brundle, 1974). Low energy photons with energy around 7 eV are capable of determining the bulk electronic state with higher energy resolution. On the other hand, higher energy photons with energies up to several hundred electron volts (eV) could also be used to determine the bulk electronic state. Furthermore, the polarizations of the incident photons provides a new degree of freedom in ARPES measurements, enabling us to selectively probe the electrons from orbitals with different symmetries. Thus, a beamline which can cover low photon energy down to 7 eV and up to several hundred electron volts with variable polarizations is long-awaited in the study of condensed matter physics by means of ARPES.

A vacuum ultraviolet (VUV) beamline (BL03U) has been built at the Shanghai Synchrotron Radiation Facility (SSRF), and has been designed for ARPES experiments with a photon energy range of 7–798 eV. It is rather challenging to generate 7 eV photons at SSRF, because the energy of the storage ring is as high as 3.5 GeV. In this case a deflection parameter K of greater than 10 is required and the heat load would be a serious problem (Hofmann, 2004). To solve this problem, an APPLE-Knot undulator was adopted, which can generate
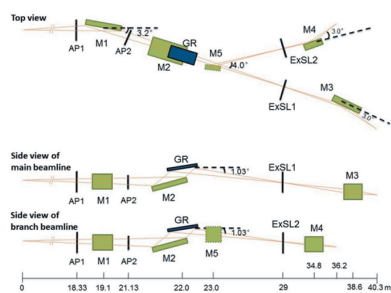
photons with variable polarizations and low on-axis heat load (Ji *et al.*, 2015). In this paper, we report the design and performance test of this beamline.

2. Layout of the beamline

A schematic layout of the beamline is shown in Fig. 1 and the parameters selected are given in Table 1. In Fig. 1, the zero point of the coordinates is set as the center of the undulator. The photon beam generated from the APPLE-Knot undulator is first focused horizontally onto the exit slit by an elliptical cylindrical mirror M_1 (19.1 m) and deflected by 3.2° in the horizontal direction. Apertures set before (18.33 m) and after (21.13 m) M_1 are used to control the acceptance angle of the photon beam. A plane mirror M_2 is used to reflect the beam upwards toward the gratings (22 m). After the varied-line-space plane grating (VLPG) (Harada *et al.*, 1984; Itou *et al.*, 1989; Yan *et al.*, 1998), the photon beam is focused onto the exit slit (29 m) vertically. The plane mirror M_5 (23 m) set after the monochromator is used to switch the photon beam to pass the main or branch line. After the exit slit, the photon beam is refocused in both the horizontal and vertical directions by an ellipsoidal mirror (M_3 at 38.6 m or M_4 at 34.8 m for the main or branch line, respectively). The total length of the beamline from source to sample position is 40.3 m or 36.2 m for the main or branch line, respectively.

For better thermal conductivity, most of the optical elements (M_1, M_2, gratings, M_5) are made of silicon. Also, a conventional side-cooling system was adopted for M_1, M_2 and the grating. The ellipsoidal mirrors M_3 and M_4 are made of silicon dioxide as they are at the end of the beamline where the heat load is negligible. All of the optical elements are coated with Au. Table 2 shows the parameters of the ellipsoidal mirrors. Since M_1 is the first mirror of the beamline with

Table 1
Parameters of the optical elements.

Element	Figure	Distance (m)	Deflection angle (°)	(R/ρ) (m)	Effective size (mm)	Size (mm)
M1	Elliptical cylindrical	19.1	3.2	14.50 / 0.38	411×30	425 × 40 × 50
M2	Plane	21.93–21.65	20.97–4.57		352 × 18	362 × 40 × 50
G1	VLSPG	22.00	158–174.4		127 × 9	137 × 30 × 50
G2	VLSPG	22.00	158–174.4		127 × 9	137 × 30 × 50
G3	VLSPG	22.00	158–174.4		72 × 9	85 × 30 × 50
M3	Elliptical	38.6	3.0	5.65 / 0.11	435 × 48	435 × 61 × 90
M4	Elliptical	34.8	3.0	3.60 / 0.07	257 × 25	270 × 40 × 60
M5	Plane	23	4.0		200 × 30	215 × 40 × 60

Table 2
Elliptical mirrors parameters.

Element	Slope error (µrad)	Roughness (nm)	Coating material	Coating thickness (nm)
M1	0.2	0.3	Au	30
M3	10.0	0.5	Au	30
M4	2.0	0.3	Au	30

long entrance arm (source to M_1, 19.1 m) and exit arm (M_1 to exit slit, 9.9 m), it has higher requirements regarding slope error and roughness.

2.1. Undulator

The beamline is served from Section 03U of the SSRF. As a photon source, a 4.2 m-long APPLE-Knot undulator was put into practical use for the first time. Unlike conventional undulators, APPLE-Knot undulators can provide photons with arbitrary polarizations and a much lower on-axis heat load. According to simulations, the heat loads of the APPLE-Knot undulator are 59.4, 43.9 and 314 W for horizontal, circular and vertical modes, respectively, inside the 0.6 mrad × 0.6 mrad acceptance solid angle, which is satisfactory compared with 1106 W for a pure linear undulator (Ji *et al.*, 2015). First-order light covers the photon energy range 7–165 eV, and higher harmonics could be used to provide higher-energy photons.

The effective electron beam size σ_{r0} and divergence σ'_{r0} of the storage ring of SSRF in the vertical (horizontal) direction are 8.36 µm (143.2 µm) and 4.18 µrad (34 µrad), respectively. Then, from consideration of the spatial coherence (diffraction limit), the r.m.s. of size σ_r and divergence angle σ'_r of the source are (Onuki & Elleaume, 2003)

$$\sigma_r = \left(\sigma_{r0}^2 + \frac{1}{2\pi^2} \lambda L \right)^{1/2}, \tag{1}$$

$$\sigma'_r = \left(\sigma_{r0}'^2 + \frac{\lambda}{2L} \right)^{1/2}, \tag{2}$$

where λ and L are the wavelength of the photon and the total length of the undulator, respectively. The above equations give us the σ_r and σ'_r values at the harmonic energy. However, for certain acceptance angles, the flux peak energy is lower
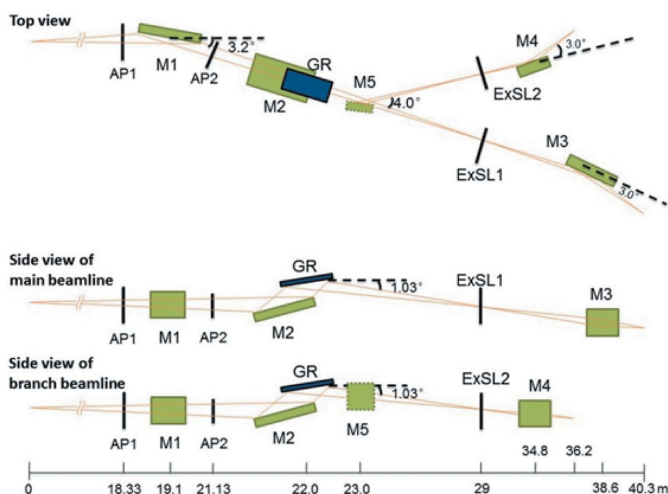

Figure 1
Schematic layout of beamline 03U.

Table 3
Comparison of the vertical source sizes obtained by two methods.

Photon energy	σ_{v0}	σ_v
21.6 eV	110.8 μm	70.7 μm
48.4 eV	74.3 μm	46.0 μm
65.0 eV	64.3 μm	41.6 μm

Table 4
Grating parameters.

Grating	k_0 (mm^{-1})	Energy range	b_2 (10^{-4} mm^{-1})	b_3 (10^{-8} mm^{-2})	$-\alpha$ (°)	β (°)
G1	188	7–103 eV	1.705	2.296	84.01–88.52	73.99–85.87
G2	620	17.3–246 eV	1.512	2.107	85.69–89.03	72.31–85.37
G3	2000	56–798 eV	1.514	2.109	85.66–89.02	72.34–85.38

than the harmonic energy and the r.m.s. of the source size at peak energy (σ_v) is smaller than that calculated by equation (1) (σ_{v0}) (Onuki & Elleaume, 2003). In order to solve this problem we use the *SPECTRA* program (Tanaka & Kitamura, 2001) to calculate the source sizes at flux peak energies. Table 3 shows a comparison of the source sizes obtained by the two methods at three different photon energies corresponding to the gas absorption edges. One can clearly see that the source sizes at peak energy σ_v are significantly smaller than those at resonance energies σ_{v0} by 30–40%.

2.2. Monochromator

In order to achieve good efficiency of the gratings, *i.e.* as high as possible for different photon energies and a small beam size at the sample position, we choose a variable-groove-depth (VGD) and a variable-line-space plane-grating in the design of the monochromator (VLPGM). The design principles of the VLPGM, as well as its advantages compared with other types of monochromators, have been described in detail earlier (Reininger & Castro, 2005; Wang *et al.*, 2015). Therefore only a brief description of the geometry and optical elements used in this design is given below. Three Au-coated gratings with line densities of 188, 620 and 2000 lines mm^{-1} are used, covering the energy range 7–798 eV. Further details of these gratings are listed in Table 4. To obtain high flux, low-line-density gratings (188 lines mm^{-1}) are used, and consequently the diffraction limitation takes an important role in the energy resolution. To decrease the contribution from the diffraction limitation, the monochromator parameters are carefully selected, and almost the same illuminated length, which is also the effective grating length, on the grating can be achieved for different photon energies, which also means that the maximum incident angles or, say, the maximum reflectivity has been achieved for the whole energy range. Suppose the line density of the VLPGM is

$$k = k_0\left(1 + 2b_2w + 3b_3w^2\right), \quad (3)$$

where the positive direction of w is along the photon propagation direction, then the grating diffraction and the focus condition for the -1 order (inner order) diffraction are

$$\sin\alpha + \sin\beta = -\lambda k_0, \quad (4)$$

$$\frac{\cos^2\alpha}{r} + \frac{\cos^2\beta}{r'} - 2b_2k_0\lambda = 0, \quad (5)$$

where r, r' are distances between the grating and source and exit slit, and λ is the photon wavelength. According to equations (4) and (5), each photon wavelength corresponds to a

set of incident angle (α) and diffraction angle (β). Therefore, photons of different energies can be delivered to the exit slit through the coordinated rotation of M_2 and the grating. When the values of r and r' are different from the theoretical ones, the focus condition can be remedied by the change of α and β achieved by the rotations of the pre-mirror (M_2) and grating, which is another advantage of the VLPGM. The vertical magnification of the grating is

$$M_G = \frac{\cos\alpha/r}{\cos\beta/r'}. \quad (6)$$

To keep the fixed direction of the exit photons, the M_2 mirror needs both translational and rotational movements. This complex movement can be achieved by an off-axis rotation of M_2. As shown in Fig. 2, the distance between the entrance light and the rotation center of the grating is set as 28 mm. The best performance is achieved when we set the rotation axis of M_2 at $(-0.02\ \text{mm}, 14.41\ \text{mm})$ referring to the grating center, and the movement of the beam center on the grating surface is shorter than 20.6 μm during the energy scan.

3. Theoretical performance from beamline design

Firstly, we estimate the energy resolution of the beamline by considering the contribution from the source size, diffraction limitation, slope error of M_2, slope error of the grating and coma focus, which could be calculated using the following equations,

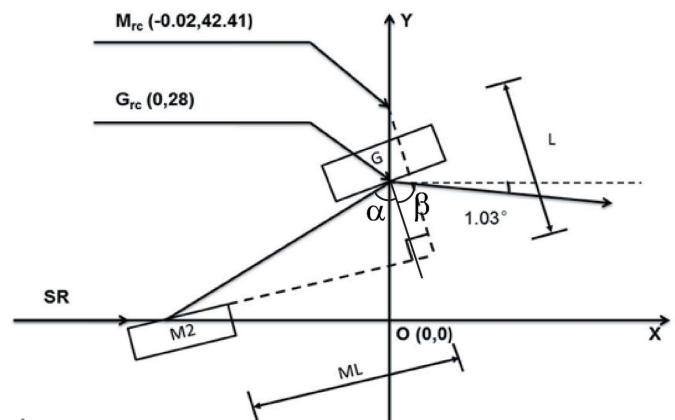$$\left(\frac{\Delta E}{E}\right)_{so} = \frac{2.35\sigma_v\cos\alpha}{\lambda k_0 r}, \quad (7)$$

Figure 2
Geometry of the M_2 rotation mechanism.

$$\left(\frac{\Delta E}{E}\right)_{\text{slit}} = \frac{\sigma_s \cos \beta}{\lambda k_0 r'}, \qquad (8)$$

$$\left(\frac{\Delta E}{E}\right)_{\text{diff}} = \frac{1}{k_0 l} = \frac{\cos \alpha}{k_0 4 \sigma_v' r}, \qquad (9)$$

$$\left(\frac{\Delta E}{E}\right)_{\text{sm}} = \frac{2.35 \times 2\sigma_m}{\lambda k_0} \cos \alpha, \qquad (10)$$

$$\left(\frac{\Delta E}{E}\right)_{\text{sg}} = \frac{2.35 \sigma_g}{\lambda k_0} (\cos \alpha + \cos \beta), \qquad (11)$$

$$\left(\frac{\Delta E}{E}\right)_{\text{coma}} = \left(\frac{2.35 \times 0.5 \sigma_v' r}{\cos \alpha}\right)^2 \frac{3 F_{30}}{2 \lambda k_0}, \qquad (12)$$

where σ_v, σ_s, l, σ_v', σ_m and σ_g are the vertical source size, vertical width of the exit slit, illuminated length, vertical source divergence, mirror slope error and grating slope error, and

$$F_{30} = \frac{\sin \alpha \cos^2 \alpha}{r^2} + \frac{\sin \beta \cos^2 \beta}{r'^2} - 2\lambda k_0 b_3. \qquad (13)$$

Here, F_{30} is set to zero at the midpoint of the energy range covered by each grating by choosing a suitable b_3. In the calculations, the vertical source sizes (σ_v) are obtained using the *SPECTRA* program as listed in Table 3. The slope errors of the gratings and M_2 are selected as the measured values from real optics of this beamline, which are 0.12 µrad, 0.13 µrad and 0.14 µrad for G1, G2 and M_2, respectively. Fig. 3 shows the total energy resolution calculated by the above equations for a 10 µm vertical width of the exit slit. One can see that grating 2 has a better energy resolution and its energy resolution reaches below 0.5 meV of the full width at half-maximum (FWHM) at the photon energy 21.6 eV, in which most contributions are from the diffraction limitation (0.31 meV), the vertical width of the exit slit (0.30 meV) and the source size (0.24 meV), and the others can be ignored.

The parameters chosen for each grating are shown in Table 4, and the photon fluxes at the sample position of the three gratings are shown in Fig. 4, calculated using the code *REFLECT* (Schäfers *et al.*, 2002). As exhibited in Fig. 4, all three gratings could reach fluxes of more than 10^{13} photons s^{-1} (0.1% bandwidth)$^{-1}$ in the photon energy range 7–100 eV. In the calculations, the ring current is set as 300 mA, which is that of SSRF at full state.

4. Beam delivery performance

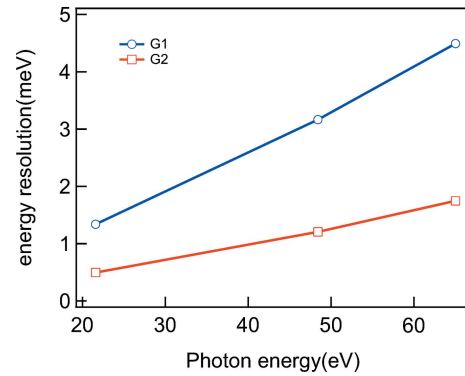The energy resolution of the monochromator was tested by performing gas-phase photoabsorption measurements on He and Ne. The gas cell employed in these studies was mounted behind the post-focusing mirror (M_3). A perforated plate valve with thin film was used to isolate the gas from the ultrahigh vacuum (UHV), and the thickness of the Al film was 150 nm, and is transparent to photons in the photon energy range 20–70 eV. The pressure of the gas was set to approximately 5×10^{-2} mbar as measured using a Pirani vacuum gauge. A photodiode of type AXUV100G (Opto-Diode Corporation, California, USA) inside the gas cell was used to measure the photon intensity I. The photocurrent generated on M_3 was used as the initial current I_0. In the gas absorption spectrum scan, the minimum energy step was set at 0.05 meV, which was close to the driving limit of the stepper motor of M_2 and the grating, which is 75 nrad step^{-1}, corresponding to 0.01 meV. The experiments were carried out at room temperature with horizontally polarized light. The results of the photoabsorption (I/I_0) for different gases are displayed in Fig. 5. Here only the photoabsorption spectra of G_2 with line density 620 lines mm^{-1} are illustrated. More test results of other gratings are listed in Table 5.

Figure 3
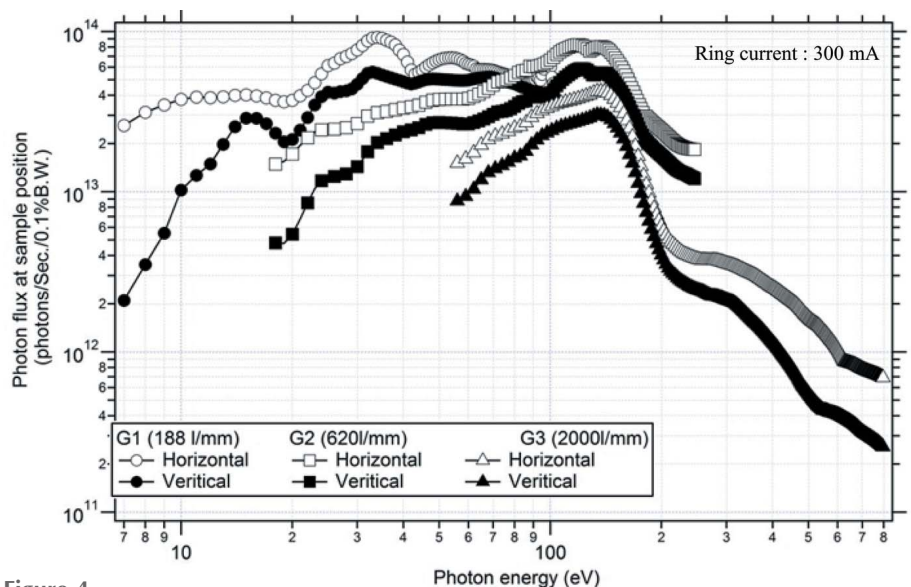Theoretical energy resolution at three photon energies.

Figure 4
Theoretical photon flux at the sample position with horizontally polarized and vertically polarized light. Circles, squares and triangles represent gratings G1, G2 and G3, respectively.

Table 5
Resolving power and flux of the monochromator for the vertical width of the exit slit of *10 µm / 30 µm (the ring current is 240 mA).

Energy	Resolving power (G1)	Resolving power (G2)	Flux (G1) [photons s⁻¹ (0.1% bandwidth)⁻¹]	Flux (G2 [photons s⁻¹ (0.1% bandwidth)⁻¹]
21.6	*15354 / 14250	*45953 / 30813	2.91×10^{13}	*1.21×10^{13} / 2.34×10^{13}
48.6	*18956 / 9890	*47488 / 20305	2.66×10^{13}	*2.15×10^{13} / 2.63×10^{13}
65.5	*12462 / 8350	*31238 / 15589	1.68×10^{13}	2.13×10^{13}
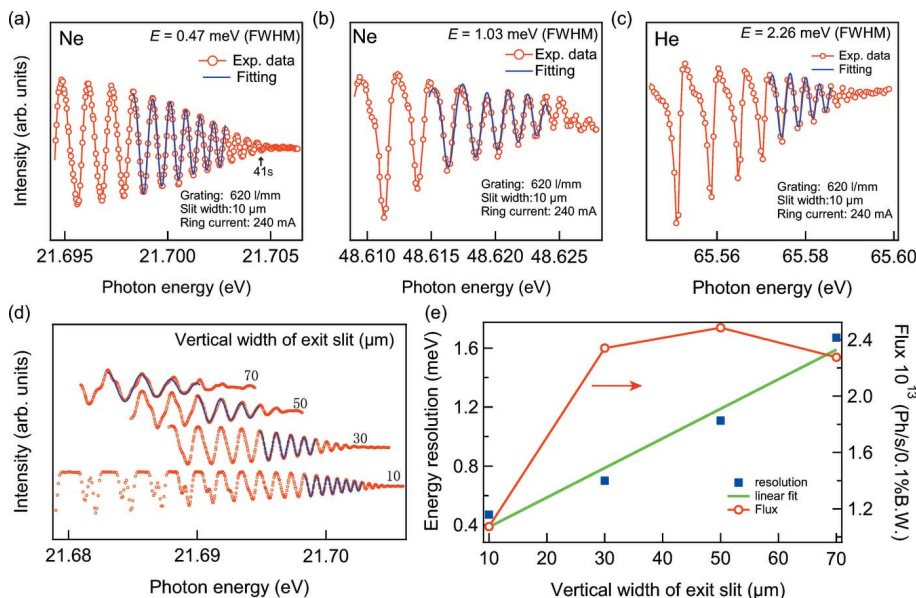
Figure 5
(a, b) Ne and (c) He absorptions for 10 µm vertical width of the exit slit and G2. The red open circles and blue solid lines represent the experimental data and multi-peak fittings, respectively. (d) Experimental data and multi-peak fittings of absorptions with different vertical widths of the exit slit (10, 30, 50, 70 µm). (e) Fluxes and energy resolutions with different vertical widths of the exit slit. All data are measured using horizontal polarized light with 240 mA ring current.

The photoabsorption spectra with different photon energies are shown in Figs. 5(a)–5(c) with the vertical width of the exit slit being 10 µm. The experimental resolution was estimated by a multi-peak fitting method [equation (14)], and the standard deviation σ of the energy distribution of the incident monochromatic light could be obtained,

$$A = A_0 \sum_{n=-\infty}^{\infty} \exp\left[-\frac{(x_n - x)^2}{2\sigma^2}\right], \qquad (14)$$

where x_n is the position of the nth peak. An energy resolution (FWMH = 2.35σ) of 0.47 meV was achieved at 21.6 eV, corresponding to a resolving power of $E/\Delta E = 4.6 \times 10^4$. Similarly, the resolving powers for photon energies at 48.6 eV and 65.5 eV are 4.7×10^4 and 3.1×10^4, respectively [Figs. 5(b)–5(c)]. Fig. 5(d) shows a typical series of Ne spectra at a photon energy of 21.6 eV with different vertical widths of the exit slit. The multi-peak fittings are shown as blue curves in Fig. 5(d) and the results are presented as blue squares in Fig. 5(e). One can see that the energy resolution changes linearly with the vertical width of the exit slit.

The photon flux on the samples is measured using an AXUV100G photodiode downstream of mirror M_3. The diode response was calibrated using a standard curve from the diode manufacturer, Opto Diode Corporation. The resulting calibrated photon fluxes for different vertical widths of the exit slit are also shown on the right-hand axis of Fig. 5(e), with 240 mA ring current. As the vertical width of the exit slit becomes larger, the energy resolution becomes linearly worse and the received photons increase linearly, which leads to basically an unchanged photon flux, that remains above 2.2×10^{13} photons s⁻¹ (0.1% bandwidth)⁻¹ when the vertical width of the exit slit is above 30 µm. The photon flux drops by half when the vertical width of the exit slit is adjusted to 10 µm because the energy resolution is no longer linearly proportional to the slit width and also other factors (such as the diffraction limitation) become major contributions to the energy resolution as discussed before.

More experimental results of the resolving power and flux for different gratings are exhibited in Table 5. It is worth noting that the resolving power of G2 remains above 4.6×10^4 with a flux of over 10^{13} photons s⁻¹ (0.1% bandwidth)⁻¹ in the photon energy range 21–48 eV. The resolving powers of G1 and G2 are slightly decreased when the photon energy is above 48 eV, which is consistent with the previous theoretical calculations. The measured photon flux is approximately $(1.6–2.9) \times 10^{13}$ photons s⁻¹ (0.1% bandwidth)⁻¹ for the 188 lines mm⁻¹ grating (G1) and $(2.1–2.6) \times 10^{13}$ photons s⁻¹ (0.1% bandwidth)⁻¹ for the 620 lines mm⁻¹ grating (G2) in the energy range 21–65 eV. Considering that the ring current is 240 mA during the test, the flux would increase accordingly when the ring current is in a 300 mA full state. Overall, the measured results show good agreement with the estimated values.

Next, we tested the performance of the beamline in delivering low-energy photons. The higher harmonic contamination of the photon beam becomes a serious problem when very low energy photons are used. Fig. 6(a) shows the photoemission spectrum with 7.2 eV photon energy. One can see that the higher harmonics give a huge background and that the first-order light of 7.2 eV is submerged in it. To solve this problem, we use a 200 µm-thick CaF_2 filter at the end of the beamline.

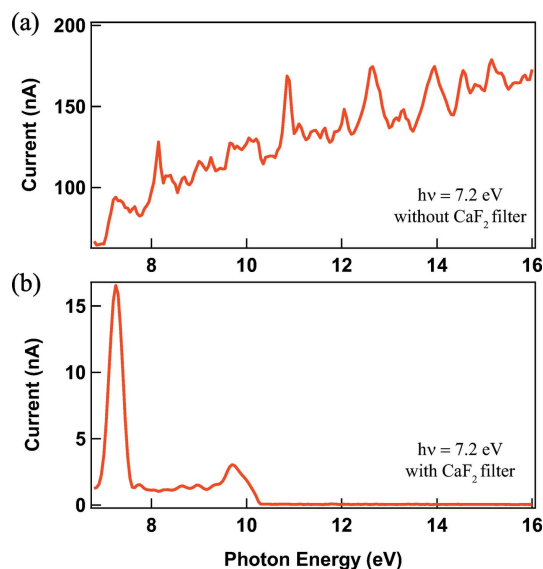As shown in Fig. 6(*b*), the harmonics with photon energy above 10 eV are rejected and the first-order light at 7.2 eV shows a sharp fine shape. After the CaF$_2$ filter, the peak current from the photodiode at 7.2 eV photon energy is reduced to 1.65×10^{-8} A and the corresponding photon flux is 1.54×10^{11} photons s^{-1}. The theoretical energy-resolving power is about 8000 when the photon energy is 7.2 eV (Wang *et al.*, 2015), thus the normalized photon flux is 1.23×10^{12} photons s^{-1} (0.1% bandwidth)$^{-1}$. The photon flux of 7.2 eV is one order of magnitude lower than that of 21.6 eV. Because the photoionization cross section of the valence band increases dramatically with the decrease of photon energy, the ARPES experiments of low-energy photons still have a high enough efficiency.

Finally, we tested the size of the focused beam at the sample position, since a sufficiently small spot size is critical to guarantee excellent angular resolution of photoelectrons in state-of-the-art ARPES measurements. Fig. 7 exhibits the experimental vertical and horizontal spot sizes at the sample position when the vertical width of the exit slit is set as 30 µm with 21.6 eV photon energy. The experimental data were collected by measuring the first-order derivation of the photocurrent from a square aperture scanning vertically and horizontally, respectively, yielding a spot size of 7.5 µm (V) × 67 µm (H) FWHM. The vertical size of the spot at the sample position is determined by the width of the exit slit and M_3. Since M_3 remains unchanged, the vertical size of the spot can be changed through the change of the width of the exit slit, while the horizontal size of the spot at the sample position is determined by the original source size of the undulator, M_1 and M_3. According to equation (1), the source size decreases as the photon energy increases, and theoretically the horizontal size of the spot at the sample position would decrease accordingly. However, we found that the horizontal size of the spot at the sample position is almost unchanged as the photon
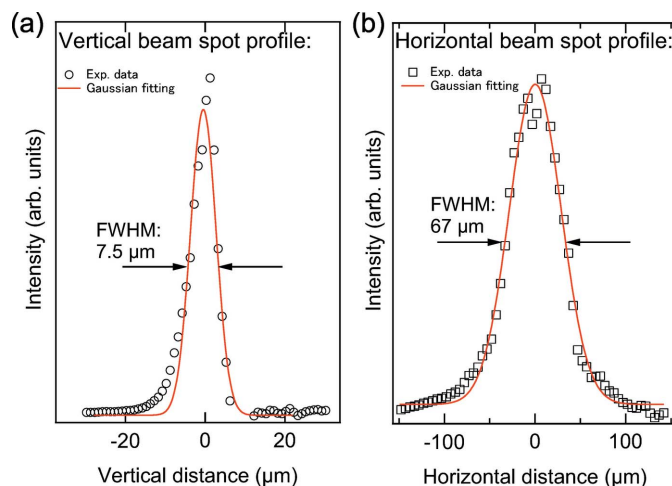
energy increases, which is due to the slope error of M_3 playing a major role in the influence of the spot size at the sample position.

5. Summary

The vacuum ultraviolet beamline BL03U has been constructed and commissioned at SSRF for ARPES experiments. The beamline is equipped with an APPLE-Knot undulator and three VGD-VLP gratings, covering the photon energy from 7 eV upwards with variable polarizations and much lower heat load. The beamline delivers photons with a resolving power exceeding 4.6×10^4 and flux up to 10^{13} photons s^{-1} (0.1% bandwidth)$^{-1}$ in the range 21–48 eV, when the ring current is 240 mA. The beam sizes at the sample position are 7.5 µm FWHM and 67 µm FWHM in the vertical and horizontal directions, respectively. The energy resolution and beam size at the sample both meet the design expectations, and the ARPES endstation of BL03U has been opened to users.

References

Brundle, C. R. (1974). *J. Vac. Sci. Technol.* **11**, 212–224.

beamlines

Damascelli, A., Hussain, Z. & Shen, Z. (2003). *Rev. Mod. Phys.* **75**, 473–541.

Harada, T., Itou, M. & Kita, T. (1984). *Proc. SPIE*, **0503**, 114–118.

Hofmann, A. (2004). *The Physics of Synchrotron Radiation.* Cambridge University Press.

Itou, M., Harada, T. & Kita, T. (1989). *Appl. Opt.* **28**, 146–153.

Ji, F., Chang, R., Zhou, Q., Zhang, W., Ye, M., Sasaki, S. & Qiao, S. (2015). *J. Synchrotron Rad.* **22**, 901–907.

Onuki, Hideo & Elleaume, Pascal. (2003). *Wigglers, Undulators and Their Applications.* London: Taylor and Francis.

Reininger, R. & de Castro, A. R. B. (2005). *Nucl. Instrum. Methods Phys. Res. A*, **538**, 760–770.

Schäfers, F., Abramsohn, D. & Krumrey, M. (2002). *REFLEC, a Program to Calculate VUV/X-ray Optical Elements and Synchrotron Radiation Beamline.* BESSY Press.

Tanaka, T. & Kitamura, H. (2001). *J. Synchrotron Rad.* **8**, 1221–1228.

Wang, J., Ye, M., Shi, T., Chang, R. & Qiao, S. (2015). *Chin. Phys. C.* **39**, 048001.

Yan, Y., Shigemasa, E. & Yagishita, A. (1998). *J. Synchrotron Rad.* **5**, 246–251.